Journal of
Marine Science and Engineering

MDPI

Article

Numerical Investigation of Depressurization through Horizontal Wells in Methane-Hydrate-Bearing Sediments Considering Sand Production

Xuyang Guo [1,*], Yan Jin [1], Jingyu Zi [1], Jiaying Lin [1], Bolong Zhu [1], Qian Wen [2] and Qi Jing [3]

[1] College of Petroleum Engineering, China University of Petroleum (Beijing), Beijing 102249, China
[2] Beijing Gas Group Co., Ltd., Beijing 100034, China
[3] Beijing Gas Energy Development Co., Ltd., Beijing 100012, China
* Correspondence: xguo@cup.edu.cn

Abstract: Sand production has been identified as a key reason limiting sustained and commercial gas production in methane-hydrate-bearing sediments. Production tests in Canada and Japan were terminated partially because of excessive sand production in pilot wells. It is meaningful to carry out numerical investigations and sensitivity analyses to improve the understanding of sand production mechanisms during the exploitation of methane hydrates. This study introduces a numerical model to describe the coupled thermal–hydraulic–mechanical–chemical responses and sand production patterns during horizontal well depressurization in methane-hydrate-bearing sediments. The model is benchmarked with a variety of methane hydrate reservoir simulators. Results show that the spatial and temporal evolution patterns of multi-physical fields are different and the hydromechanical evolutions are the fastest. Gas production and sand production rates are oscillatory in the early stages and long-term rates become stable. Gas production is sensitive to rock physical and operational parameters and insensitive to rock mechanical properties such as cohesion. In contrast, sand production is sensitive to cohesion and insensitive to rock physical and operational parameters. Although cohesion does not directly affect gas productivity, gas productivity can be impaired if excessive sand production impedes production operations. This study provides insights into the sand production mechanism and quantifies how relevant parameters affect sand production during the depressurization in methane-hydrate-bearing sediments.

Keywords: methane hydrate; numerical simulation; methane production; hydrate dissociation; depressurization

Citation: Guo, X.; Jin, Y.; Zi, J.; Lin, J.; Zhu, B.; Wen, Q.; Jing, Q. Numerical Investigation of Depressurization through Horizontal Wells in Methane-Hydrate-Bearing Sediments Considering Sand Production. *J. Mar. Sci. Eng.* **2022**, *10*, 1777. https://doi.org/10.3390/jmse10111777

Academic Editor: Timothy S. Collett

Received: 15 October 2022
Accepted: 13 November 2022
Published: 18 November 2022

1. Introduction

Methane hydrates are usually found in permafrost and marine sediments where pressures are usually high and temperatures are usually low [1]. In hydrate-stable zones, thermodynamic equilibria for methane hydrates are obtained and researchers estimated that the methane in this type of reserve can be around 10^5 TCF or up to 10^{18} ST m^3 [2–4]. Since the consumption of methane is regarded to be clean and sustained, it is meaningful to consider the possibility of developing methane from the methane-hydrate-bearing sediments. Multiple attempts have been made worldwide where production test sites were built for methane production from hydrate-bearing sediments. Vertical and horizontal wells were drilled, and the bottom hole pressures in the wells were lowered to depressurize the sediments for methane production. In some of the production tests, sand production has become a major problem preventing sustained and commercial gas production, as the produced sand can damage the pumps, block the flows in wellbores, and lead to the termination of gas production. For example, the test site in the Nankai Trough in 2013 reported 27 m^3 sand production in six days, which contributed to the termination of the test production [5–13]. Therefore, understanding the sand production mechanism in methane-hydrate-bearing sediments is very relevant as it is key for sustained and commercial methane production from hydrate-bearing sites.

Sand production is usually related to the deterioration of mechanical properties of hydrocarbon-bearing formations and sediments. It is often reported in the development of hydrocarbon resources from reservoirs. In weakly consolidated and unconsolidated formations, pressure depletion introduced in the wells alters the pressure and stress fields in the reservoirs, which can lead to sand erosion and migration [14]. During the exploitation of hydrocarbons, the coupled flow and geomechanical responses lead to rock mechanical failures and eroded sand can be produced along with hydrocarbons. Some experimental and numerical investigations have been carried out to understand the sand production behaviors in weak formations. Entering the plasticity regime was identified as a major reason for sand production in the lab carried out by Papamichos et al. [15]. Jung and Satamarina [16] and Sanchez and Satamarina [17] investigated the dilatant behaviors under shear deformation, which can cause tensile stresses when the hydrate saturations are high and confining stresses are low. These studies provided insights into the uncontrolled gas release, sand production, and submarine landslide related to methane hydrate exploitation. Based on a tri-axial test, Younessi et al. [18] indicated that mechanical failures of rocks alone cannot guarantee the production of sand particles, and minimum drawdowns are also required to initiate the sand production in wells as the drawdowns lead to pressure gradients serving as the driving force for sand production. Uchida et al. [19] identified high hydrate saturation layers are under greater shearing due to stress redistribution from layers with lower hydrate saturations, and shearing is directly related to sand production. They employed their model in the simulation of the gas hydrate production test in the Nankai Trough in 2013. Li et al. [20] presented a coupled hydromechanical model to simulate the sand production associated with erosion, where sand rates and plastic strains can be quantified. Yan et al. [21] quantified the stress concentration and strength decrease around a wellbore for methane hydrate production. They predicted the onset of sand production and analyzed the effects of temperature, stress contrast, and bottom hole pressure on sand production risks. They used equivalent plastic strain to denote the possibility of sand production. In a series of experimental and numerical investigations, Ding et al. [22] and Ding et al. [23] determined the sand yield, permeability, sand content, and productivity for methane hydrate samples from the South China Sea and proposed sand control criteria. Then, they proposed a numerical model to consider the sand produced from eroded skeletons in methane-hydrate-bearing layers. They indicated that after the initial sand production, the subsequent stage usually endures large-scale sand production. This stage may require sand control if sand production is excessive.

Previous studies of sand production often considered the quantification of geomechanical responses in the formation during hydrocarbon production. Since the depressurization in methane-hydrate-bearing sediments is a coupled process considering thermal, hydraulic, mechanical, and chemical fields, the characterization of geomechanical responses is often achieved by multi-physical modeling. Poromechanics is used to couple the fluid flow and mechanical responses, where effective stresses are induced and skeleton strength is affected [24,25]. The chemical process is mainly about the dissociation of methane hydrates. The process is related to the pressure and temperature evolutions and hydrate dissociation can reduce the strength as well [21,26]. From the perspective of thermal–hydraulic–mechanical–chemical (THMC) modeling, depressurization leads to pressure changes and hydrate dissociation. In consequence, rock mechanical properties are changed as hydrates are part of the solid phase in the sediments before the thermodynamic equilibrium is broken. During this coupled process, plasticity is obtained at the wellbore and in the near-well zones in the reservoir [27,28]. Ning et al. [29] proposed a THMC model consisting of several modules: TOUGH + Hydrate, FLAC3D, and PFC3D. They predicted the reservoir stability and sand production based on this multi-physical strategy for a South China Sea scenario. They indicated that a balance should be obtained between sand control and methane productivity. In another numerical study of the THMC behaviors during the depressurization in methane-hydrate-bearing sediments, Jin et al. [30] correlate effective stress changes with pore pressure propagation, and effective stress increases worsen the subsidence caused by methane hydrate production.

Based on the literature review, multi-physical modeling is a key strategy for the investigation of sand production mechanisms during hydrocarbon exploitation in weakly consolidated formations. The deterioration of rock mechanical properties during methane hydrate dissociation further complicates the sand production mechanism in gas hydrate development. Therefore, it is meaningful to carry out a coupled thermal–hydraulic–mechanical–chemical modeling study of the sand production behaviors and the effects of relevant parameters during the depressurization in methane-hydrate-bearing sediments. This study proposes a coupled THMC model for the prediction of sand production during depressurization in methane-hydrate-bearing sediments based on mass and heat transport in porous media, elastoplasticity, and sand erosion. Effects of relevant rock physical, mechanical, and depressurization parameters on sand production are also quantitatively studied. This study predicts methane productivity and associated sand production, which serves as reference for the optimization of methane hydrate development strategies.

2. Methodology

In this study, the evolution of pressure, temperature, displacement, and hydrate dissociation is simulated by a coupled thermal–hydraulic–mechanical–chemical model for the depressurization process in methane-hydrate-bearing sediments. The dependent variables solved in the model are pressure, water saturation, temperature, displacement, and methane hydrate saturation.

In order to characterize the fluid flow in the saturated methane-hydrate-bearing sediments, the temporal and spatial evolution of pressure and saturation is simulated. Based on mass balance and flow diffusivity, the fluid flow in saturated porous media is described by:

$$\frac{\partial}{\partial t}(\phi S_L \rho_L) + \nabla \cdot (\rho_L v_L) = s_L \tag{1}$$

$$\frac{\partial}{\partial t}(\phi S_G \rho_G) + \nabla \cdot (\rho_G v_G) = s_G \tag{2}$$

where ϕ is the porosity of sediments; S_L is the liquid saturation; ρ_L is the liquid density; v_L is the liquid velocity; s_L is the liquid mass source; S_G is the gas saturation; ρ_G is the gas density; v_G is the gas velocity; and s_G is the gas mass source. In the assumption, the aqueous phase contains water and the gaseous phase contains methane.

The gaseous and aqueous phases' velocities are very low in porous media. Therefore, Darcy's law is used to represent these velocities [31–34]:

$$v_G = -\frac{k k_{rG}}{\mu_G} \cdot (\nabla p_G + \rho_G g) \tag{3}$$

$$v_L = -\frac{k k_{rL}}{\mu_L} \cdot (\nabla p_L + \rho_L g) \tag{4}$$

where k is the permeability of the sediments; k_{rG} and k_{rL} are relative permeability terms for the two phases; μ_G and μ_L are viscosity terms for the two phases; p_G is the pressure of the gaseous phase; p_L is the pressure of the aqueous phase; and g is the gravitational acceleration.

Since the permeability terms in methane-hydrate-bearing sediments are very saturation sensitive, the permeability and relative permeability terms are further expressed as:

$$k = k_0 (S_G + S_L) \left[\frac{(1-\phi)(S_G + S_L)}{1 - \phi(S_G + S_L)} \right]^{2\kappa} \tag{5}$$

$$k_{rG} = k_{rG}^{0}\left(S_{G,e}^{*}\right)^{nG} \tag{6}$$

$$k_{rL} = k_{rL}^{0}\left(S_{L,e}^{*}\right)^{nL} \tag{7}$$

$$S_{G,e}^{*} = \frac{S_{G}^{e} - S_{G,\ res}^{e}}{1 - S_{G,\ res}^{e} - S_{L,\ res}^{e}} \tag{8}$$

$$S_{L,e}^{*} = \frac{S_{L}^{e} - S_{L,\ res}^{e}}{1 - S_{G,\ res}^{e} - S_{L,\ res}^{e}} \tag{9}$$

$$S_{G}^{e} = \frac{S_G}{S_L + S_G} \tag{10}$$

$$S_{L}^{e} = \frac{S_L}{S_L + S_G} \tag{11}$$

where κ, nL, and nG are saturation coefficients; k_{rG}^{0} and k_{rL}^{0} are relative permeability terms of gaseous and aqueous phases at endpoints; $S_{G,e}^{*}$ and $S_{L,e}^{*}$ are normalized gaseous and aqueous phases' saturations; S_{G}^{e} and S_{L}^{e} are saturations of gaseous and aqueous phases based on effective pores, where methane hydrates are part of solid phases; and $S_{G,\ res}^{e}$ and $S_{L,\ res}^{e}$ are residual saturations of gaseous and aqueous phases in effective pores [35–37].

The first law of thermodynamics is used to describe the heat transport process in methane-hydrate-bearing sediments [17,38]. Heat conduction, heat convection, and heat absorption are considered as:

$$\frac{\partial}{\partial t}[\phi E_L \rho_L S_L + \phi E_G \rho_G S_G + \phi S_{MH} E_H \rho_H + (1-\phi) E_S \rho_S] + \nabla \cdot (\boldsymbol{i}_C + \boldsymbol{i}_E) = Q \tag{12}$$

where E_L, E_G, E_H, and E_S are specific internal energy terms associated with aqueous, gaseous, hydrate, and solid phases in the sediments; ρ_H and ρ_S are hydrate and solid density terms; $\boldsymbol{i}_C$ and $\boldsymbol{i}_E$ are heat convection terms; Q is the heat sink term since the hydrate dissociation process is endothermic. Specifically, the hydrate dissociation process is represented by the Kim–Bishnoi kinetic model [39–41]. The depressurization method artificially drops the pressure in the well below the thermodynamic equilibrium in hydrate stable zones, and the pressure difference is the driving force for methane hydrate dissociation:

$$R_{MH} = -\phi k_d M_{MH}(p_e - p_G) S_{MH} \sqrt{\frac{[\phi(S_G + S_L)]^3}{2k}} \tag{13}$$

where R_{MH} is the dissociation rate of methane hydrates; k_d is the kinetic reaction rate; M_{MH} is the molar weight of methane hydrates; and p_e is the phase equilibrium pressure.

Due to the changes in pressure and temperature, the compressibility χ_i and the thermal expansive coefficient β_i of a certain phase can be expressed as:

$$\chi_i = \frac{1}{\rho_i}\left(\frac{\partial \rho_i}{\partial p_i}\right)_T \tag{14}$$

$$\beta_i = -\frac{1}{\rho_i}\left(\frac{\partial \rho_i}{\partial T_i}\right)_p \tag{15}$$

The change in the methane hydrate saturation is related to the compressibility of methane hydrate, the expansivity of methane hydrate, and the dissociation process during depressurization in the sediments. Therefore, methane hydrate saturation can be formulated as:

$$\frac{\partial \phi S_{MH}}{\partial t} + \phi S_{MH}\left(\chi_H \frac{\partial p_L}{\partial t} - \beta_H \frac{\partial T}{\partial t}\right) = \frac{s_H}{\rho_H} \tag{16}$$

where s_H is the molar sink of methane hydrates.

Previous equations address the pressure, saturation, and temperature changes introduced by the engineering intervention of depressurization in methane hydrate-bearing sediments. It also leads to geomechanical responses in the sediments, where rock failure and sanding can occur. Based on momentum balance:

$$\nabla \cdot \boldsymbol{\sigma} + \rho_b \boldsymbol{g} = 0 \tag{17}$$

where $\boldsymbol{\sigma}$ is the stress tensor; ρ_b is the bulk density; $\boldsymbol{g}$ is the vector for gravitational acceleration. Based on infinitesimal transformation, the relationship between strain $\boldsymbol{\varepsilon}$ and displacement $\boldsymbol{u}$ is:

$$\boldsymbol{\varepsilon} = \frac{1}{2}\left(\nabla \boldsymbol{u} + \nabla^{\mathrm{T}} \boldsymbol{u}\right) \tag{18}$$

During hydrate dissociation, the strength of sediments decreases. This process is quantified by the change in cohesion:

$$c = c_0 + \frac{1 - \sin \varphi_f}{2 \cos \varphi_f} \alpha S_{MH}^{\beta} \tag{19}$$

where c is the cohesion of sediments; c_0 is a reference cohesion with no presence of methane hydrates; α and β are coefficients related to methane hydrates; φ_f is the internal friction angle.

The constitutive relationship between stress and strain is expressed as:

$$\delta \boldsymbol{\sigma} = \boldsymbol{C} : \delta\left(\boldsymbol{\varepsilon} - \boldsymbol{\varepsilon}_p\right) - b \delta p \boldsymbol{I} \tag{20}$$

where $\boldsymbol{C}$ is the tensor of elasticity; $\boldsymbol{\varepsilon_p}$ is the plastic strain; b is the coupling coefficient; and $\boldsymbol{I}$ is the second-order identity tensor.

Mohr–Coulomb and Drucker–Prager models are used to characterize shear failure under elastoplastic deformation. The yield function f and the plastic potential function g are described by:

$$f = \beta_f I_1 + \sqrt{J_2} - \kappa_f \leq 0 \tag{21}$$

$$g = \beta_g I_1 + \sqrt{J_2} - \kappa_g \leq 0 \tag{22}$$

where I_1 is the first invariant for effective stress; J_2 is the second invariant for effective deviatoric stress. Failure envelope related terms are κ_f, κ_g, β_f, and β_g [42–44]. Specifically, the Mohr–Coulomb model is written as:

$$f = \tau_m' - \sigma_m' \sin \varphi_f - c\left(\cos \varphi_f\right) \leq 0 \tag{23}$$

$$g = \tau_m' - \sigma_m' \sin \varphi_d - c(\cos \varphi_d) \leq 0 \tag{24}$$

$$\sigma_m' = \frac{\sigma_1' + \sigma_3'}{2} \tag{25}$$

$$\tau_m' = \frac{\sigma_1' - \sigma_3'}{2} \tag{26}$$

where φ_d is the dilation angle; σ_1' and σ_3' are the maximum and minimum principal effective stress. Based on the Mohr–Coulomb model's coefficients and terms, the Drucker–Prager model can be written as well.

The criterion for sand production in the study considers the failure in sediments and the sand erosion caused by fluid flow [20,23,45,46]. This is a multi-step process, where failure occurs in the rock skeleton first and sand erodes due to porous media flows driven by pressure gradients. Sand erosion is calculated as:

$$\frac{\dot{m}}{\rho_s} = \lambda(1 - \phi)\sqrt{q_i q_i} \tag{27}$$

where $\dot{m}$ is the mass rate of erosion; ρ_s is the solid density; q_i is the porous media fluid flow flux in a direction; and λ is a sand production coefficient. The sand production coefficient can be rewritten as a function of plastic shear strain:

$$\lambda = \begin{cases} 0 & \varepsilon_p < \varepsilon_p^{peak} \\ \lambda_1\left(\varepsilon_p - \varepsilon_p^{peak}\right) & \varepsilon_p^{peak} < \varepsilon_p < \varepsilon_p^{peak} + \frac{\lambda_2}{\lambda_1} \\ \lambda_2 & \varepsilon_p > \varepsilon_p^{peak} + \frac{\lambda_2}{\lambda_1} \end{cases} \tag{28}$$

where ε_p is the plastic shear strain; ε_p^{peak} is the plastic shear strain at peak strength; and λ_1 and λ_2 are sand production coefficients determined empirically and calibrated experimentally.

3. Results and Discussion

3.1. Model Verification

The model is first verified against a set of numerical simulation results as in a comparative study [47,48]. In this verification, a 1-D case is simulated. The length, width, and height of the domain are 1.5 m, 1.0 m, and 1.0 m. The domain has an initial pressure of 8 MPa, an initial temperature of 6 °C, and an initial hydrate saturation of 0.5. There is no free gas in the problem. In the 1-D domain, the right boundary has no mass or heat flow while the left boundary has a constant depressurization pressure of 2.8 MPa and a constant temperature of 6 °C. Thus, the depressurization at the left boundary leads to hydrate dissociation, which causes temperature drop and pressure drop. Other key parameters used in the verification case are: the permeability is 0.3 D; the porosity is 0.3; the compressibility of pores is 5×10^{-9} 1/Pa; the grain density is 2600 kg/m^3; the specific heat of grain is 1000 J/kg/K; and the dry and wet thermal conductivities are 2 W/m/K and 2.18 W/m/K.

The simulated results after 12 h and 72 h of depressurization are shown in Figures 1 and 2. Figure 1 shows the hydrate saturation distribution in the domain after 12 h and 72 h of depressurization using 2.8 MPa at the left boundary. The hydrate dissociation front propagates with time, and the front moves to about 0.3 m away from the left boundary after 72 h. Figure 2 shows the temperature distribution after 12 h and 72 h of depressurization. The Dirichlet boundary on the left leads to a constant temperature of 6 °C. The endothermic process decreases temperature elsewhere. The simulated results from this model are similar to results generated by other models simulating the depressurization process for methane hydrates.

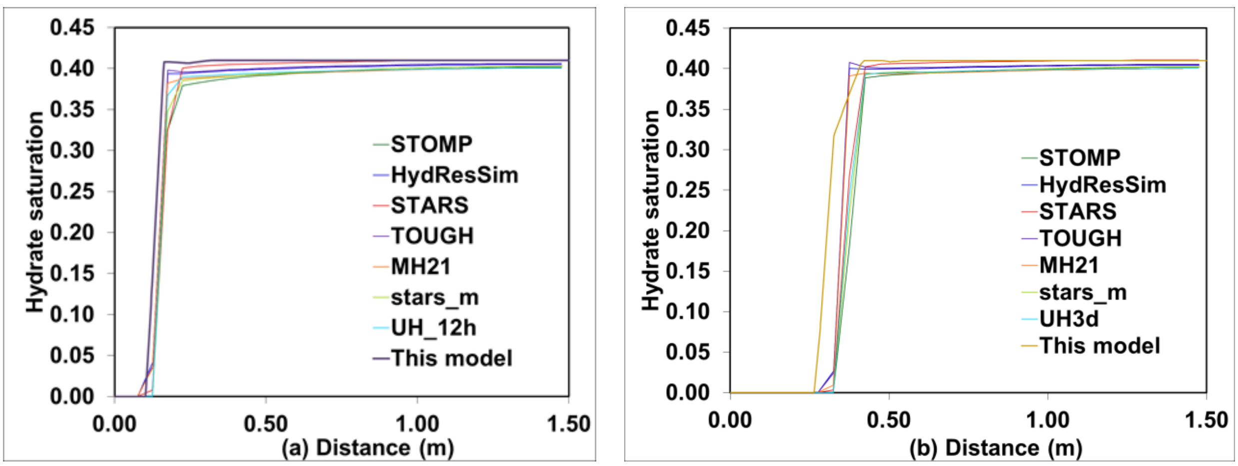

Figure 1. Hydrate saturation results compared with other simulators after (**a**) 12 h and (**b**) 72 h. Figure 2. Temperature results compared with other simulators after (**a**) 12 h and (**b**) 72 h.

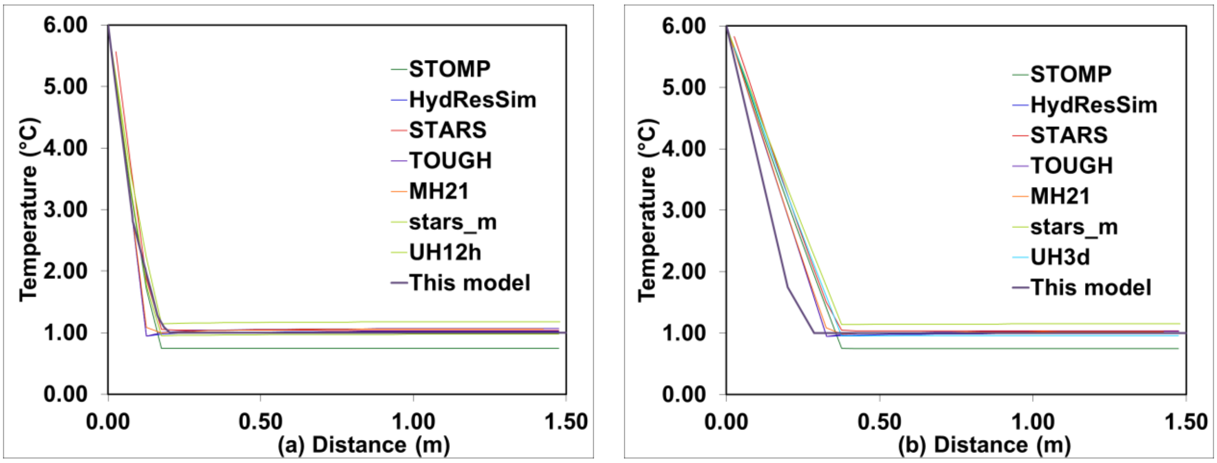

Figure 2. Temperature results compared with other simulators after (**a**) 12 h and (**b**) 72 h.

After the verification of hydrate saturation and temperature results, the sand production results are verified against lab data. The lab setup from Ding et al. [22] are reproduced in the numerical model and simulated sand production results are obtained. In Figure 3, it is noted that the simulated data are of the same order of magnitude.

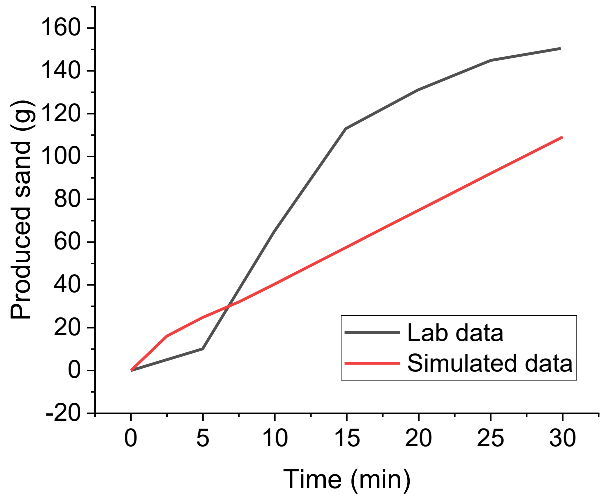

Figure 3. Comparison between the lab result [22] and the simulated result.

3.2. Base Case

A synthetic case is built for numerical analysis. As shown in Figure 4, a horizontal well depressurization scenario is considered. Due to symmetry, a two-dimensional x–z plane is simulated. The horizontal wellbore is location at x = 0 m and z = 25 m. The parameters in the model are based on several published datasets [12,13,49]. In the base case, essential simulation parameters are documented in Table 1. Since the studied layer is relatively localized, the pressure and stress gradients are neglected, while the effect of gravity on porous media flows is honored. In the x–z plane, the plane strain assumption is used.

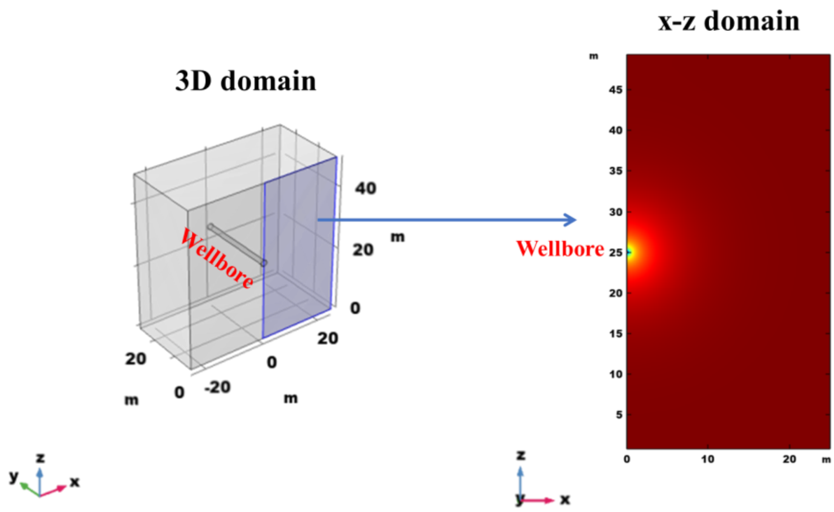

Figure 4. Dimension of the model.

Table 1. Base case parameterization.

Property	Value
Density of sediments	2300 kg/m^3
Porosity	0.15
Dry thermal conductivity	1 W/m/K
Wet thermal conductivity	3 W/m/K
Intrinsic permeability	20 mD
Initial pore pressure	14 MPa
Initial reservoir temperature	284.15 K
Initial hydrate saturation	40%
Cohesion of sediments with no hydrates	0.27 MPa
Internal friction angle	30°
Sand production coefficients λ_1 and λ_2	5 L/m and 0.005 L/m
Plastic strain at peak strength	0.024
Depressurization pressure	3 MPa
Initial stress in the x direction	14.76 MPa
Time used to reach the depressurization pressure	12 h
Depressurization time	30 days
Horizontal wellbore location	x = 0 m, z = 25 m
Dimension (x–z plane)	25 m by 50 m

In the base case, the liquid pressure distribution in the x–z domain after 1, 5, 10, and 30 days of horizontal well depressurization is plotted in Figure 5. Intuitively, the pressure values are the lowest around the wellbore, as the wellbore is prescribed with a Dirichlet boundary for pressure. After one day, the pressure in the far-field is undisturbed. As depressurization time increases, pressure depletion propagates away from the wellbore, and the pressure in the far-field starts to decrease. When the depressurization time reaches 30 days, the entire domain experiences a pressure drop. The pressure drop front expands nearly circumferentially, and a 30-day depressurization can efficiently generate pressure drop within the domain.

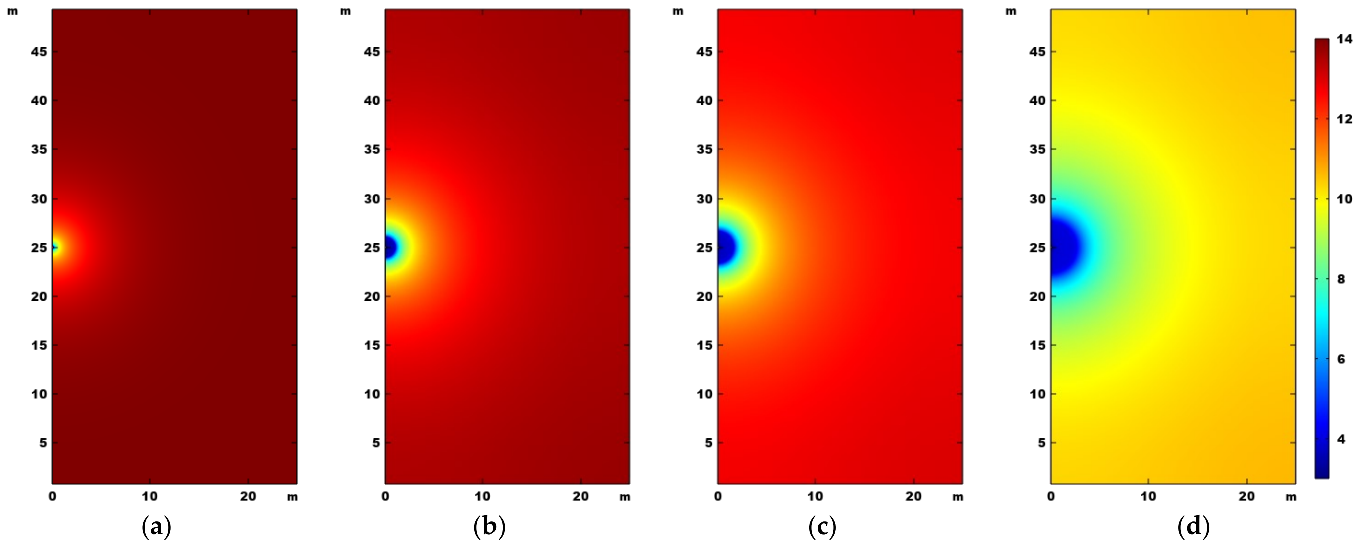

Figure 5. Liquid pressure (MPa) distribution after (**a**) 1, (**b**) 5, (**c**) 10, and (**d**) 30 days.

In Figure 6, the distribution of temperature within the domain is plotted. After one day of depressurization, the change in temperature is not significant and the temperature drop is barely noted in the domain. This is because the hydrate dissociation process on the first day is not significant, and the associated endothermic process is preliminary. After five days of depressurization, the temperature change becomes more noticeable, and the temperature drop front can be clearly observed in the near-well area. The temperature distribution results on days 10 and 30 show that the temperature drop front moves gradually with depressurization time. It is also noted that the temperature drop fronts are sharp at the four different time steps, indicating that the effect of heat absorption is relatively localized. Compared with Figure 5, although both temperature drop and pressure drop fronts are nearly circumferential, it can be noted that the temperature drop front travels much slower than the pressure drop fronts.

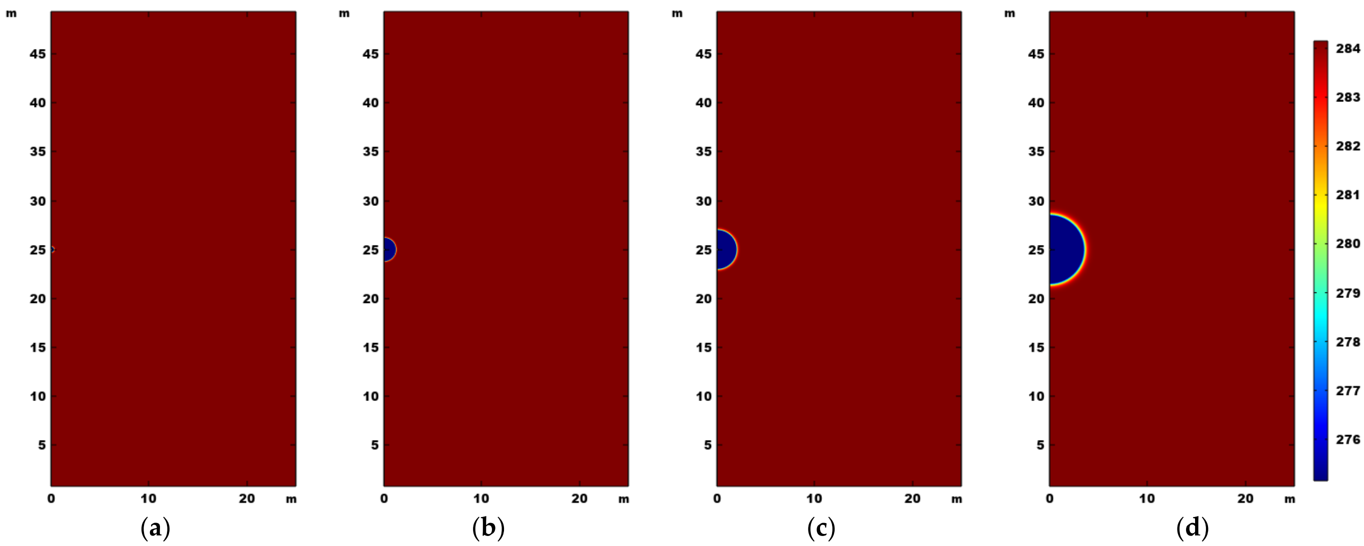

Figure 6. Temperature (K) distribution after (**a**) 1, (**b**) 5, (**c**) 10, and (**d**) 30 days.

The hydrate saturation distribution in the x–z domain after horizontal well depressurization is shown in Figure 7. It is noted that the hydrate saturation changes are sharp, corresponding to hydrate dissociation fronts. After one day, the hydrate saturation change is not clearly observed; after five days, the hydrate saturation change becomes noted, indicating that the hydrate dissociation front is gradually propagating. When the depressurization time increases to 10 and 30 days, the corresponding hydrate dissociation fronts move further. Based on the comparison between Figures 6 and 7, it can be noted that the hydrate dissociation fronts move slower than temperature drop fronts. This is because the hydrate dissociation process absorbs heat even before hydrates are completely dissociated, and the areas beyond hydrate dissociation fronts can experience temperature drops. In the x–z plane, the hydrate saturation drop fronts are also nearly circumferential as for temperature and pressure drop fronts. This is because the hydrate dissociation process is strongly coupled to the thermodynamic changes in the domain, while the thermodynamic changes are induced by horizontal well depressurizations.

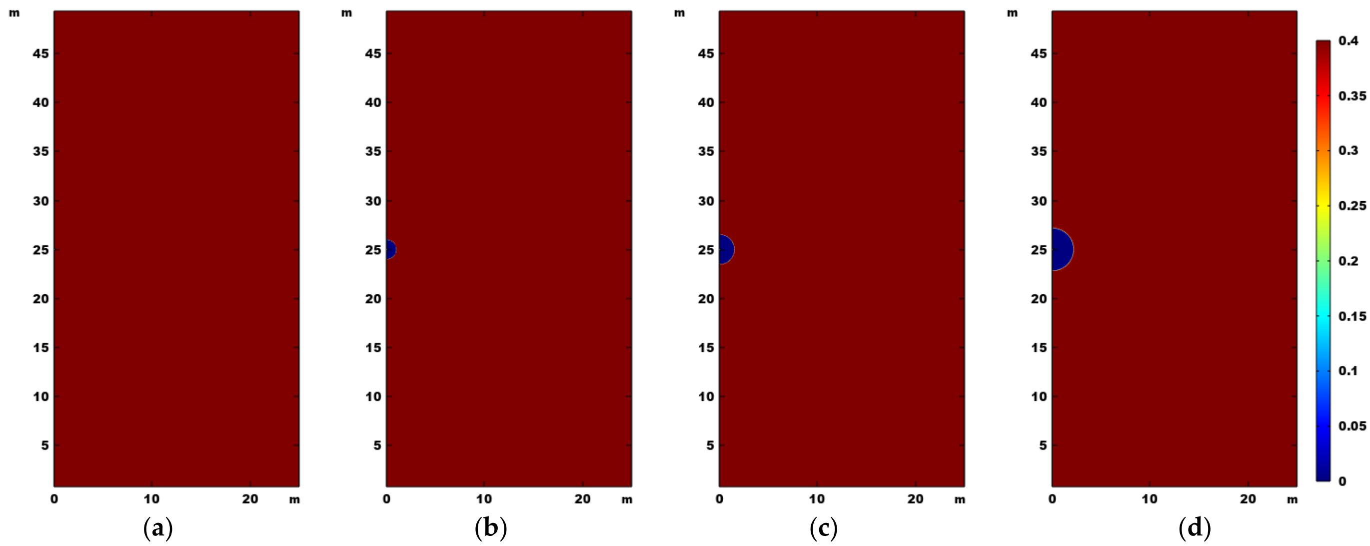

Figure 7. Hydrate saturation distribution after (**a**) 1, (**b**) 5, (**c**) 10, and (**d**) 30 days.

Since the depressurization process in methane-hydrate-bearing sediments is a coupled process, the depressurization-induced geomechanical changes are also reported. In Figure 8, stresses in the x direction S_x are plotted on days 1, 5, 10, and 30. Since the reported stress is total stress, it includes terms of pressure and effective stress in the x direction. Results indicate that the near-well areas have decreased S_x, which is caused primarily by the significant decrease in pressure.

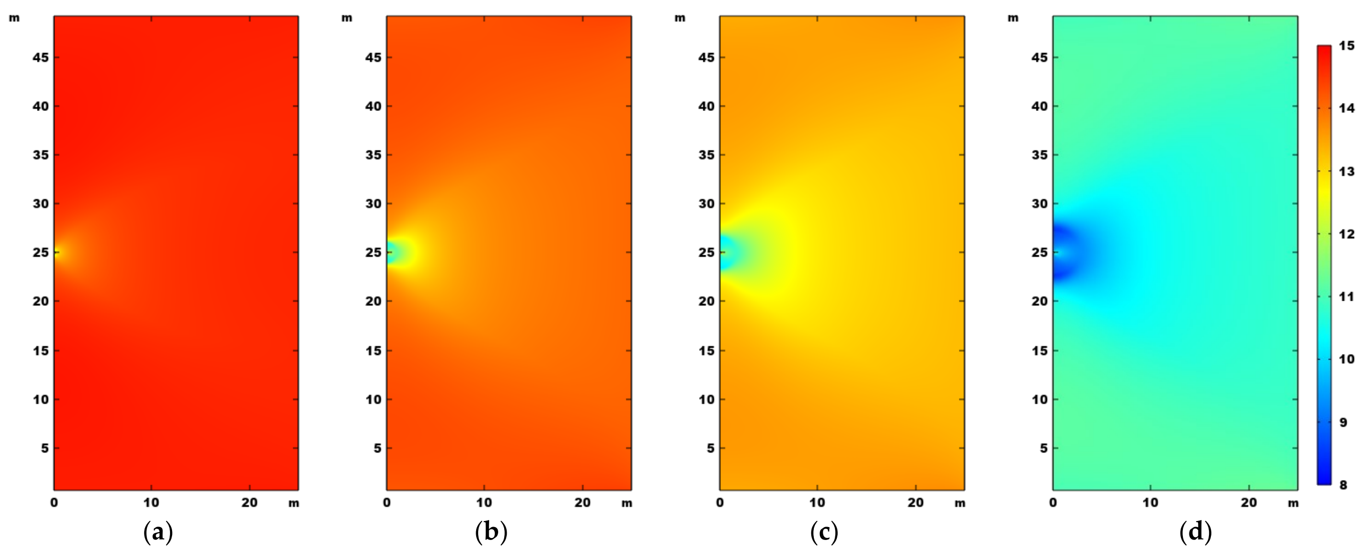

Figure 8. S_x (MPa) distribution after (**a**) 1, (**b**) 5, (**c**) 10, and (**d**) 30 days.

Since the effective stress in the x direction $S_x{}'$ is a key component in the total stress term, Figure 9 presents the distribution of $S_x{}'$ at different depressurization time steps. Results show that, regardless of depressurization time, far-field areas experience insignificant effective stress increases. In contrast, near-well areas exhibit strong depressurization-induced effective stress changes. Compared with Figure 7, areas experiencing significant effective stress changes are generally overlapped with hydrate dissociation areas, where the coupled flow and geomechanical effects are the strongest. It is also noted that at the end of the simulation, effective stress distributions at the near-well areas are slightly decreased. This is explained by the dissociated hydrates in these near-well areas, where rock strengths are damaged and skeletons withstand smaller effective stresses. This comparison indicates that hydrate dissociation is directly related to the decrease in the sediments' capability to withstand loading.

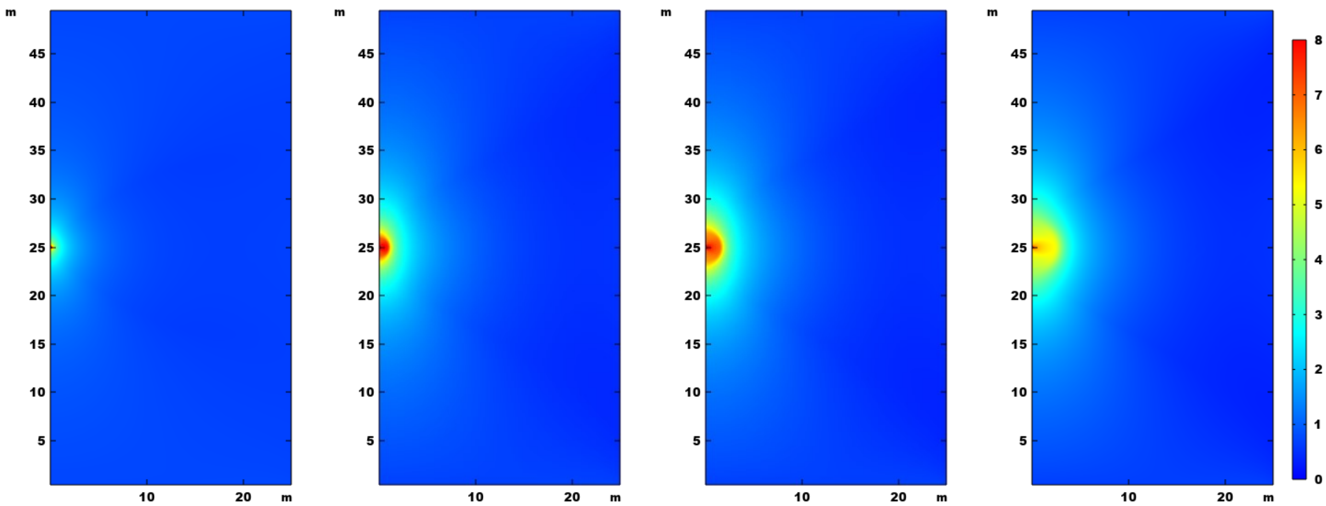

(**a**) (**b**) (**c**) (**d**)

Figure 9. $S_x{}'$ (MPa) distribution after (**a**) 1, (**b**) 5, (**c**) 10, and (**d**) 30 days.

To better present the distribution of dependent variables within the x–z domain, one-dimensional line plots are provided along z = 25 m and along x = 0 m as shown in Figure 4. Note that the plastic volumetric strain is obtained as the trace of the plastic strain tensor, and it is used to quantify the permanent deformation volumetrically. Figure 10 shows the 1D distribution of temperature, hydrate saturation, and volumetric strain for plasticity along z = 25 m, and the distribution is in the x direction. The temperature distribution curves directly present the temperature drop fronts on days 1, 5, 10, 20, and 30. It shows that the temperature changes are sharp and the endothermic process is drastic. After 30 days, the temperature drop front moves to about 4 m away from the horizontal wellbore. The hydrate saturation curves indicate the extent of hydrate dissociation. A depressurization period of 30 days makes the hydrate dissociation front move around 2 m away. Moreover, areas with hydrate dissociation are not as extensive as those with temperature drops, as heat transport can happen beyond the dissociation fronts of methane hydrates. The volumetric strain is also plotted along the one-dimensional domain for the five different time steps in a semi-log plot. Specifically, plastic strain results are evaluated volumetrically, which implies permanent deformation caused by the exploitation of methane hydrates in the sediments. In the results, as time increases, plastic volumetric strain monotonically increases, and the wellbore has the highest plastic volumetric strains due to drastic physical changes. As it moves away from the horizontal wellbore, permanent deformation becomes less significant. The curve on day one indicates that the plastic strain is zero beyond x = 20.5 m. Plastic strains on days 5, 10, 20, and 30 are all non-zero, indicating that permanent deformation is observed in the entire domain. Plastic strain curves have sudden changes at locations corresponding to hydrate dissociation fronts, indicating that hydrate dissociation has a direct impact on plastic deformation in sediments.

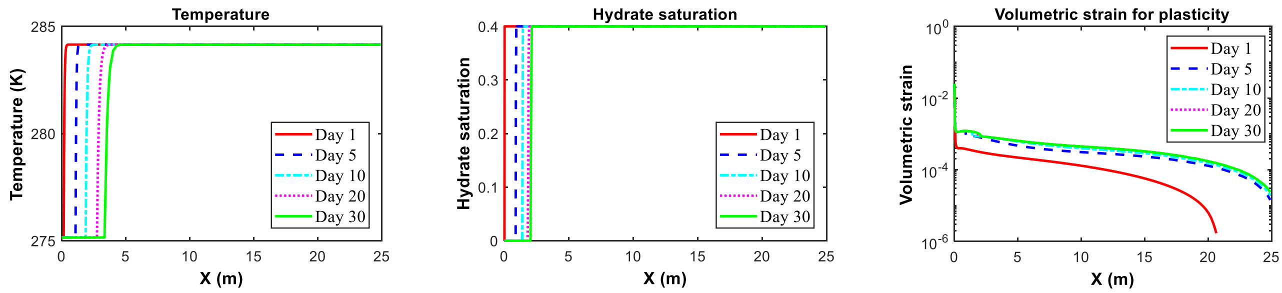

Figure 10. 1D distribution of temperature, hydrate saturation, and plastic volumetric strain along y = 25 m on days 1, 5, 10, 20, and 30.

Figure 11 shows the one-dimensional distribution of temperature, hydrate saturation, and plastic volumetric strain along x = 0 m. Thus, the changes in relevant variables at various depths can be quantified. As in Figure 4, a smaller z value indicates a greater depth. Compared with temperature and hydrate saturation curves in Figure 10, it can be observed that the distances temperature drop fronts and hydrate dissociation fronts travel at specific time steps are similar in x and z directions, which corresponds to the circumferential patterns in Figures 6 and 7. The gravity effects on temperature and hydrate saturation are not significant. However, the plastic volumetric strain curves in the z direction are different from those in the x direction. On days one and five, plastic volumetric strain values tend to be greater at shallower depths. This is affected by gravity, as areas above the horizontal wellbore have greater pressure depletion while areas below the wellbore have weaker pressure depletion. Based on poromechanical relationships, smaller pressure changes correspond to weaker mechanical responses. In addition, in the z direction, plastic deformations are not as extensive as those in the x direction.

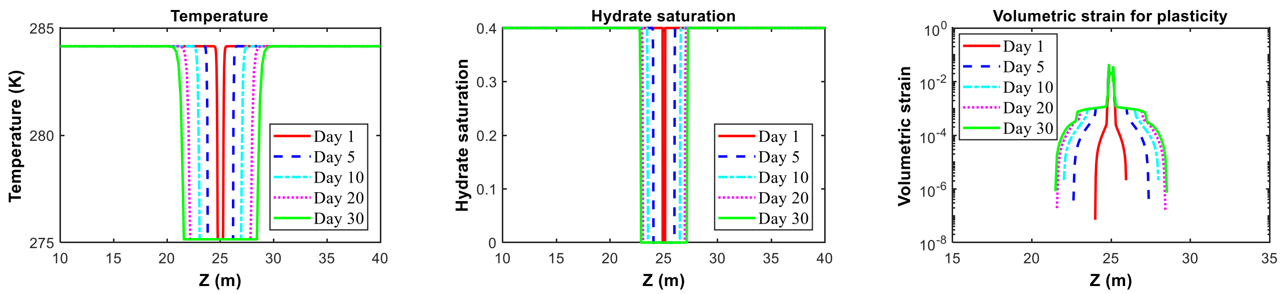

Figure 11. 1D distribution of temperature, hydrate saturation, and plastic volumetric strain along x = 0 m on days 1, 5, 10, 20, and 30.

Figure 12 shows the gas production and sand production in the base case. Since a two-dimensional simulation is conducted, the production rates are prescribed in a plane. Gas rates are plotted with a semi-log scale. During the 30-day production, the gas production rate increases significantly in the first several days. Gas production rates then drop rapidly, and they become relatively stable in the end. Sand production rates reach their peak in the first days. The greatest sand rate reaches 32 kg/m/d, which corresponds to a daily sand production of 0.014 m^3 per meter of the horizontal wellbore. Then, sand rates fluctuate between 16 kg/m/d and 29 kg/m/d. Afterward, sand rates monotonically decrease and finally reach a stable level. Gas and sand production rate results indicate that, due to the complicated coupling nature between the thermal, hydraulic, mechanical, and chemical processes during depressurization in methane hydrates, gas and sand rates are not monotonically decreasing with time. They are jointly affected by the multi-physical process. As a reference, the Mallik site reported 5 m^3 sand production in about 24 h, and the Nankai Trough site reported 27 m^3 sand production in 6 days. The well in the Mallik case has a producing interval of 12 m and the Nankai Trough case has a producing interval of about 40 m [13,50]. If these results are normalized to 2D, the normalized Nankai Trough sand rate is 259 kg/m/d and the normalized Mallik sand rate is 958 kg/m/d. The sand rate in this study is lower than the that of the Mallik and Nankai Trough cases, and it is in accordance with the observation in Ye et al. [12] that insignificant sand production was reported.

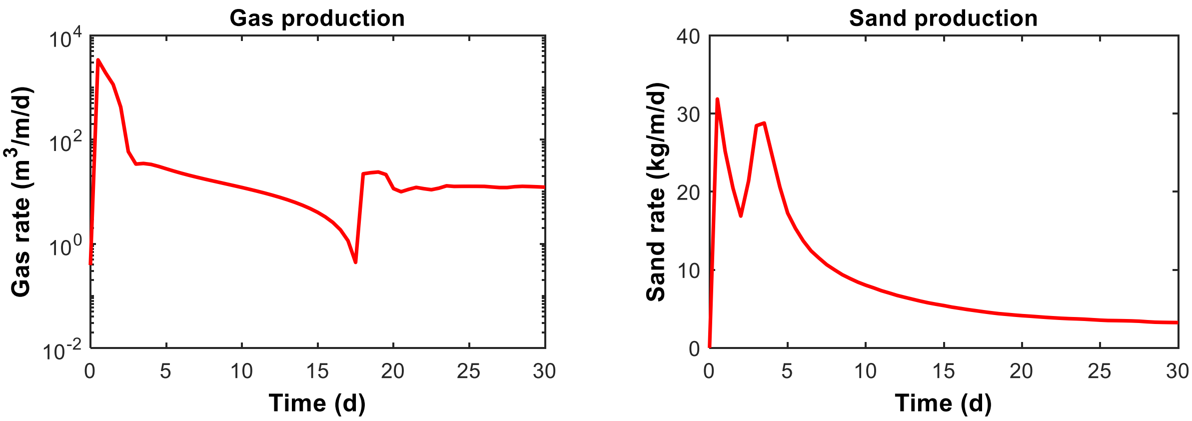

Figure 12. Gas production and sand production in the base case.

3.3. Sensitivity Analyses

After the discussion of the results in the base case, sensitivity analyses are carried out to quantify the effects of relevant modeling parameters on the coupled THMC behaviors and sand production patterns. The considered parameters include permeability, cohesion, and time used to reach depressurization pressure in the wellbore. In each investigation, only the studied parameters are changed while other parameters are the same as the base case. The sensitivity analyses can provide insights into the effects of reservoir physical, mechanical, and operational parameters on sand production.

3.3.1. Effect of Permeability

Permeability is a critical physical property for hydrocarbon-bearing formations. It governs the capability to flow in porous media. In this study, a 2 mD permeability was investigated in the base case. Additionally, another two permeability values of 1 mD and 3 mD are simulated so that the effect of permeability on the coupled THMC responses along with gas and sand production can be quantified.

Figure 13 shows the distribution of hydrate saturation, temperature, and plastic volumetric strain in the x direction after 1, 10, and 30 days of depressurization. They are plotted along z = 25 m where the horizontal wellbore is located. Semi-log plots are used for plotting the curves. After one day, hydrate dissociation is nearly nonexistent, and the hydrate dissociation fronts barely move on the semi-log scale. On days 10 and 30, the effects of permeability on hydrate dissociation fronts are not significant. Similarly, although temperature drop fronts move away from the horizontal wellbore with time, the temperature drop is not significantly affected by permeability neither. This is because hydrate dissociation front movement and heat transport are closely related to the endothermic hydrate dissociation process, and this process is less affected by permeability. Permeability governs the fluid flow within the porous hydrate-bearing sediments, while it is not directly coupled with the kinetics of hydrate decomposition. The plastic volumetric curves indicate that, after one day of depressurization, the effects of permeability in near-well areas are insignificant. Note that areas with no plastic deformation do not have plastic volumetric strain values plotted in the curves. In contrast, in the scenario with the highest permeability, the plastic region is the most extensive, and the scenario with the lowest permeability has the smallest plastic region. This is because a higher permeability leads to a faster pressure drop front movement, which causes a strongly coupled flow and mechanical response in the sediments. This indicates that the effect of permeability on plasticity is primarily observed in the far field. As depressurization time increases to 10 and 20 days, this effect largely weakens. Another phenomenon is that the plastic volumetric curves exhibit stepwise patterns, and the steps basically correspond to the hydrate dissociation fronts. This is because hydrate dissociation weakens the strength of the skeletons in sediments, which makes it easier for the solid phase to enter plasticity. In consequence, areas beyond hydrate dissociation fronts have smaller plastic strains, implying that undissociated areas have less permanent damage caused by depressurization.

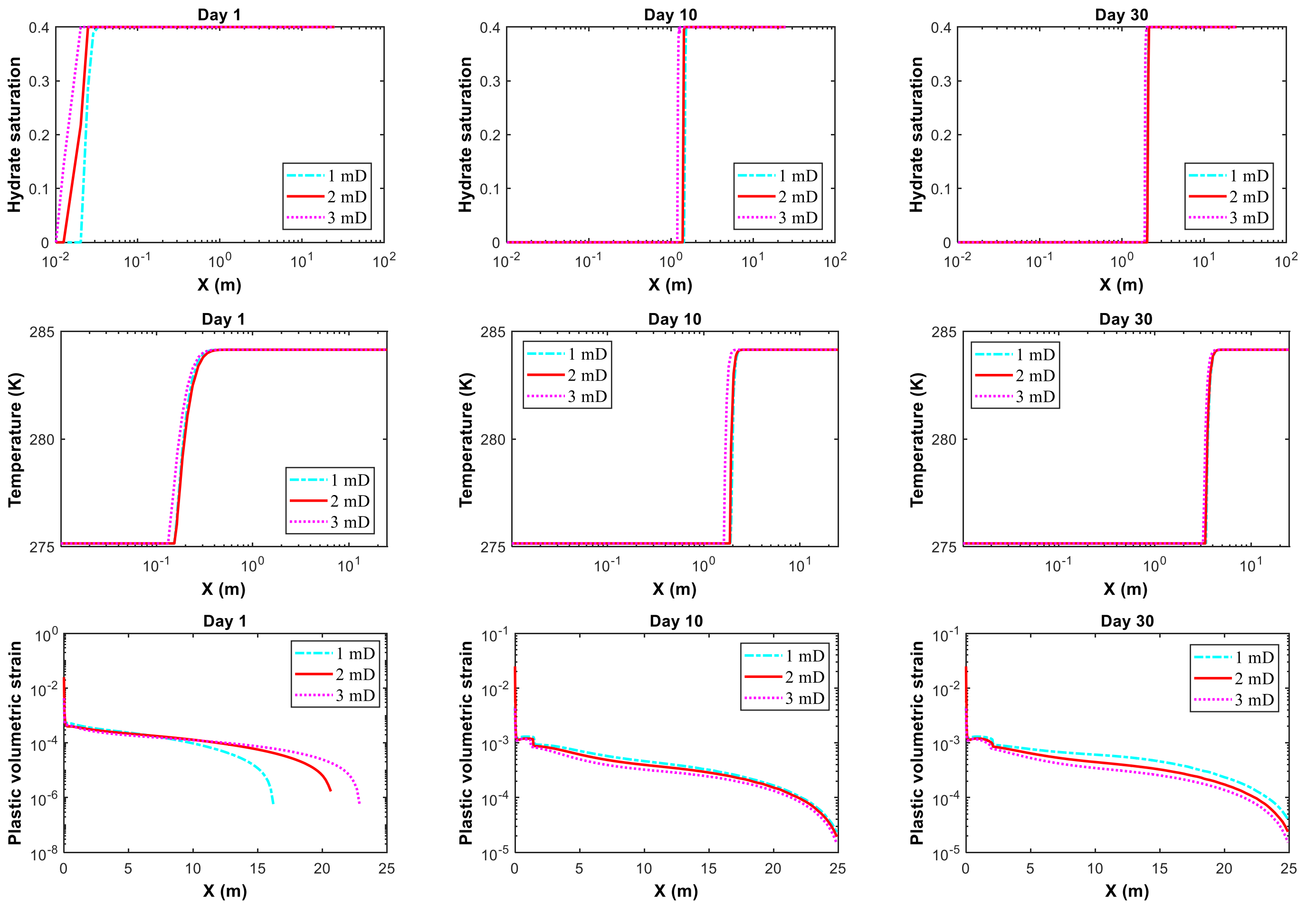

Figure 13. Effects of permeability on hydrate saturation, temperature, and plastic volumetric strain on different time steps.

In Figure 14, the effects of permeability on gas production rate and sand production rate are compared. Permeability affects the gas production trends. When the permeability is 1 mD, the gas production rate peaks right after the beginning of depressurization and drops to a relatively stable one. As the permeability value increases to 2 mD and 3 mD, there is a temporary sudden decrease in the gas rate before it finally becomes stable. This can be explained by the fact that a higher permeability results in faster hydrocarbon drainage in near-well areas with dissociated hydrates. If the drainage of methane is faster than the generation of methane from hydrate dissociation, a sudden decrease in gas production rate can occur. Specifically, the occurrence of this sudden decrease in the 3 mD scenario is earlier than in the 2 mD scenario. This is because a 3 mD permeability leads to stronger hydrocarbon drainage than the 2 mD scenario. Since permeability does not have a significant impact on hydrate dissociation, the two permeability scenarios have very similar hydrate dissociation rates. Therefore, faster methane drainage makes the sudden decrease in gas rate occur earlier. The Cartesian plot for gas rates in Figure 14 can better exhibit the significant effect of permeability on early-stage gas production performance.

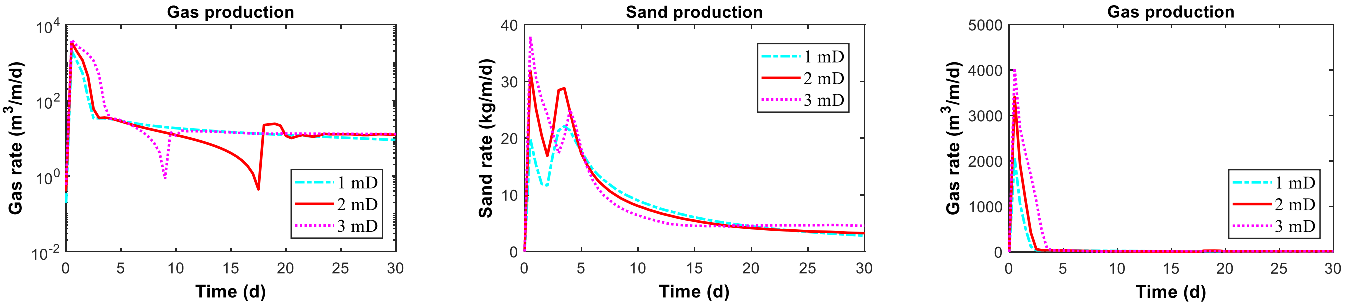

Figure 14. Effects of permeability on gas (semi-log and Cartesian) and sand (Cartesian) production rates.

Effects of permeability on sand production are more significant in the early stages, and the 1 mD permeability scenario has the lowest early-stage sand production profile. In contrast, the 3 mD permeability scenario has the highest early-stage sand production rates. This is because a higher permeability means faster pressure changes, which induced stronger geomechanical responses and plastic damage. Since the production of sand is jointly affected by rock failure and porous media flow, the 3 mD permeability scenario has the strongest plastic damage and sand erosion, and it provides the greatest pressure drawdown for sand to move. The 3 mD permeability scenario also leads to the highest long-term sand production rate, meaning that the effect of permeability on sand production exists during the entire depressurization timeframe.

It is concluded that the effects of permeability on gas and sand rates are significant at earlier stages, while gas and sand rates at final stages are not largely affected. It is also noted that horizontal well depressurization in hydrate-bearing sediments with lower permeability values can lead to weaker sand production rates and less serious sand control problems.

3.3.2. Effect of Cohesion

Cohesion is an important rock mechanical property denoting the strength of solids. In the analysis, three cohesion values of 0.135 MPa, 0.27 MPa (base case), and 0.54 MPa are investigated. The cohesion values here are for the property of the skeleton in the sediments without methane hydrates. The existence of methane hydrates can improve the overall strength of hydrate-bearing sediments. Figure 15 shows the effect of cohesion on hydrate saturation, temperature, and plastic volumetric strain in the x direction at z = 25 m. Several depressurization time steps including 1, 10, and 30 days are presented. Hydrate saturation and temperature curves show that the effect of cohesion on the spatial and temporal evolutions of the hydrate dissociation fronts and the temperature drop fronts is insignificant. This is because hydrate dissociation and temperature changes are directly governed by the thermodynamic changes caused by pore pressure depletion, and cohesion is not directly involved in this process. Comparatively, the effect of cohesion on the spatial and temporal evolutions of plastic deformation can be observed. After one day of depressurization, the plastic region with cohesion of 0.54 MPa is the smallest as the highest cohesion of the skeleton makes it hard to enter plasticity. For scenarios with cohesions of 0.27 MPa and 0.135 MPa, plastic regions on day one expand, and the 0.135 MPa scenario even has the entire domain entering plasticity after the first day of depressurization. After 10 and 30 days of depressurization, the plastic deformations with cohesions of 0.135 MPa and 0.27 MPa further expand, and the plastic volumetric strain values increase as well. At these times, only the 0.135 MPa cohesion scenario has elastic regions in the far field, indicating that a high cohesion delays the propagation of the plastic region. The plastic volumetric strain curves also exhibit stepwise behaviors, indicating that regions beyond hydrate dissociation fronts withstand smaller plastic deformations.

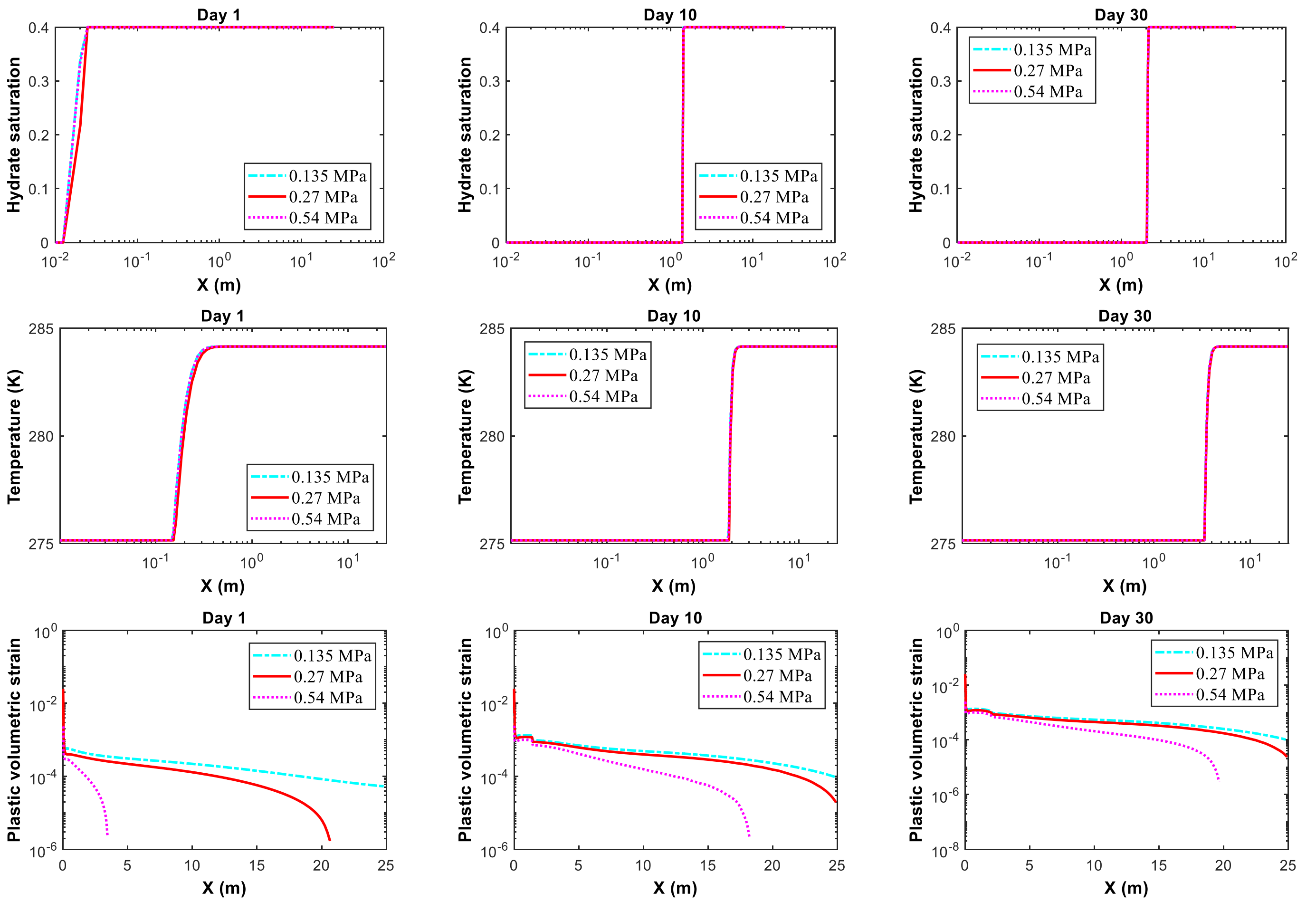

Figure 15. Effects of cohesion on hydrate saturation, temperature, and plastic volumetric strain on different time steps.

Figure 16 compares the gas and sand production rates in scenarios with several studied cohesions. The gas production rate curves show that there is a nearly negligible effect of cohesion on gas production trends, as cohesion is more related to the geomechanical responses than the thermodynamic process. However, it is observed that the effect of cohesion is significant on the sand production trends. In the scenario with the highest cohesion of 0.54 MPa, the peak sand production rate is the lowest in all three scenarios. The stable sand production rate after 5 days is relatively low. In contrast, the other two scenarios with smaller cohesion values have higher sand production rates, and after the peak sand production in the early stages, the 0.135 MPa cohesion scenario has the highest overall sand production curve of the cohesion scenarios. It indicates that the effect of cohesion on sand production exists in both the short term and the long term. Results indicate that sand production is sensitive to the rock mechanical property of cohesion.

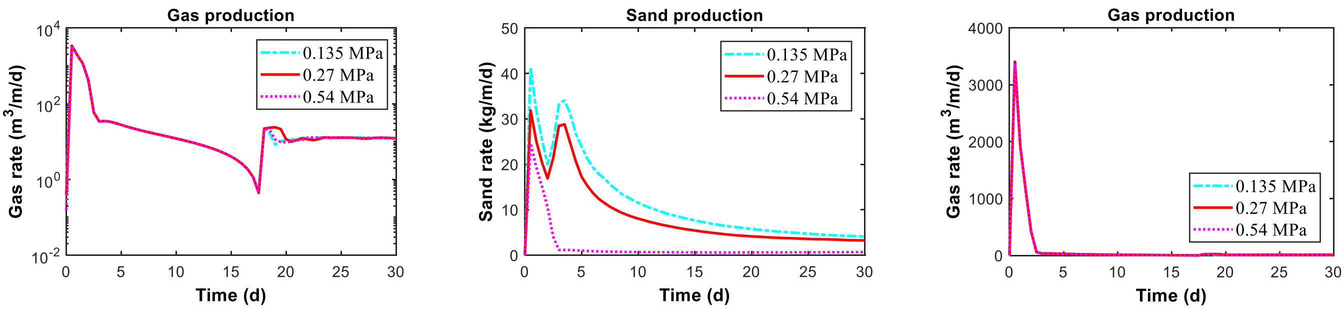

Figure 16. Effects of cohesion on gas (semi-log and Cartesian) and sand (Cartesian) production rates.

3.3.3. Effect of Time to Reach Depressurization

Depressurization through wellbores is a typical strategy in the engineering intervention for methane hydrate exploitation. Pumps are usually involved in this process to drop the bottom hole pressure to a desirable value to establish depressurization. The time used to reach the desired depressurization pressure in the bottom hole can range from a few hours to several days [12,51]. Since the effect of the time to reach depressurization and its correlation with sand production has not been studied, this investigation compares the coupled THMC behaviors and the resulting gas and sand production rates in three scenarios. The durations used to reach depressurization are 6 h, 12 h, and 24 h.

Figure 17 shows that the time to reach depressurization on the temporal and spatial evolutions of hydrate saturation, temperature, and plastic volumetric strain mainly takes effect on the first day of depressurization, while its effect is negligible on other days. When the duration is 24 h, it results in the slowest hydrate dissociation, temperature drop, and the smallest plastic region. In this scenario, the pressure depletion is the slowest on the first day. When the duration is 6 h, the THMC behaviors are the strongest in the three scenarios. Therefore, the thermodynamic changes and geomechanical responses are negatively correlated with the time to reach the depressurization pressure in the early stages.

In Figure 18, it is noted that although the effect of time to reach depressurization is significant on the first day, its effect on the gas and sand production curves can be affected in a prolonged manner. The peak gas production rate in the 24 h scenario is reached slower than the other two scenarios, as the highest gas production rate is usually obtained after the establishment of the depressurization process. It is also noted that the 6 h scenario has the most significant gas rate drop after 17 days, as the 6 h depressurization strategy has the strongest early-stage hydrocarbon drainage. The sand production curves indicate that, while the overall sand production profiles are shifted by the time to establish depressurization, the oscillatory patterns and ranges of sand rates are very close. Therefore, although the effect of time to reach the depressurization pressure can be quantified by the sand rate curves, its effect on the magnitude of sand production is relatively limited.

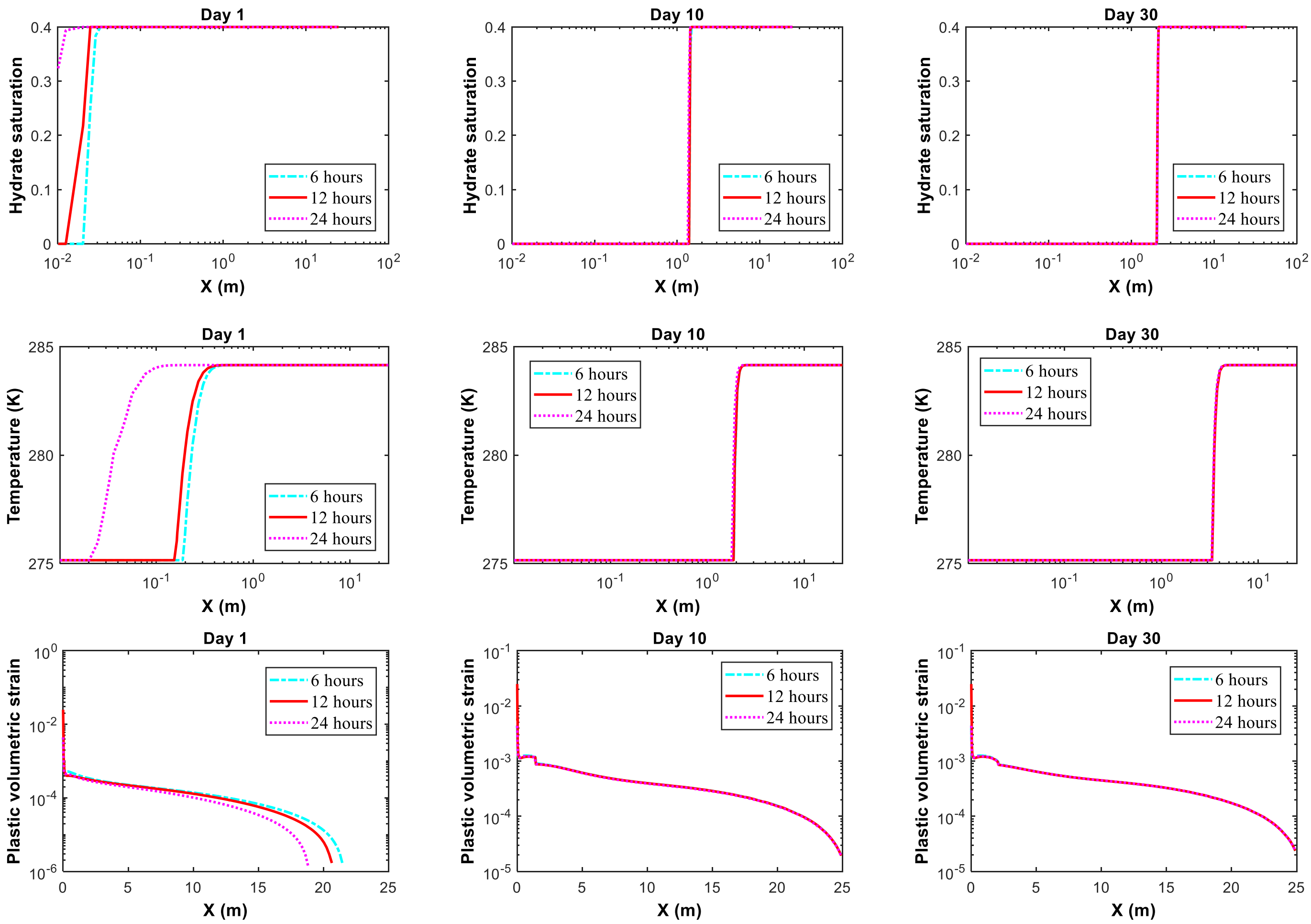

Figure 17. Effects of time used to reach depressurization on hydrate saturation, temperature, and plastic volumetric strain on different time steps.

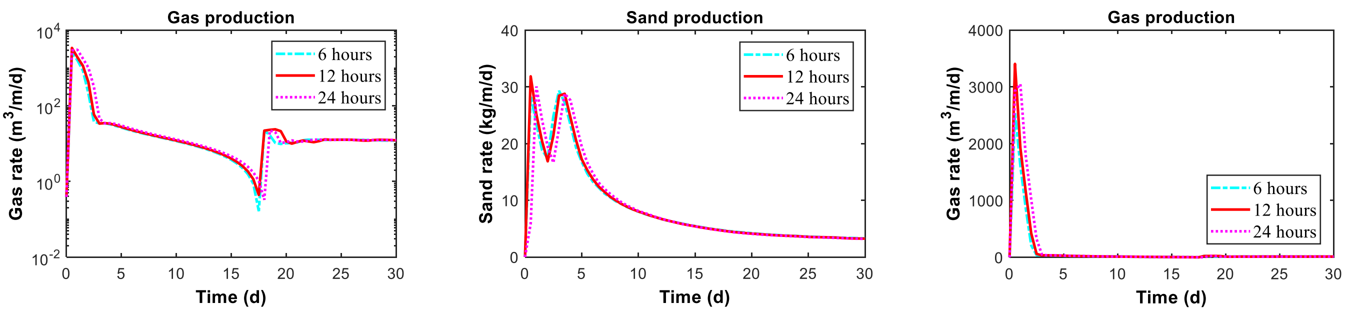

Figure 18. Effects of time used to reach depressurization on gas (semi-log and Cartesian) and sand (Cartesian) production rates.

3.4. Discussion

Results in the base case and sensitivity analyses quantify the coupled THMC behaviors and gas and sand production performance during the depressurization in methane-hydrate bearing sediments. Based on the quantitative analysis, the THMC responses and production behaviors are usually not simply monotonical and they are jointly affected by multiple physical fields. To better present the sensitivity, Figures 19 and 20 are plotted to correlate the investigated parameters with cumulative sand production and cumulative gas production at certain discrete depressurization time steps. Cumulative sand production is not very sensitive to permeability or time to reach the depressurization pressure, as these two parameters directly govern pressure depletion and thermodynamic processes which are not tightly coupled with geomechanical responses including the failure and sand erosion. In contrast, sand production is highly sensitive to cohesion, as it directly controls the yield criterion in Mohr–Coulomb and Drucker–Prager models. Based on the same logic, cumulative gas production is sensitive to permeability and time to reach the depressurization pressure, while it is very insensitive to cohesion. This is because the geomechanical behaviors are induced by depressurization, and the evolution in the geomechanical field does not significantly affect the fluid flow in porous media in return.

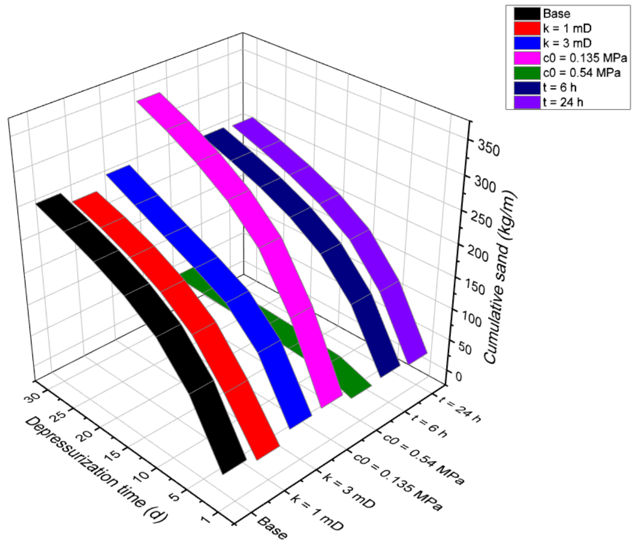

Figure 19. Sensitivity of cumulative sand production to investigated parameters.

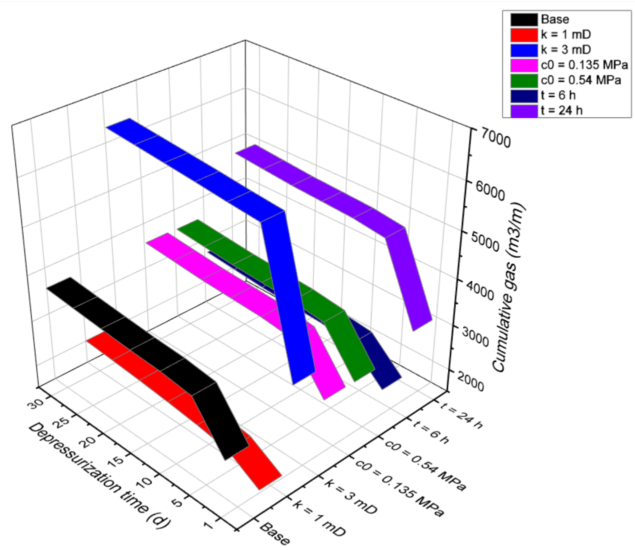

Figure 20. Sensitivity of cumulative gas production to investigated parameters.

Based on the analysis, on the one hand, it is meaningful to accurately measure the cohesion in the target sediments as it is a critical index for the quantification of the risk of sand production. In this numerical study, a cohesion of 0.54 MPa can guarantee that the sand production is contained at a relatively low level, while a cohesion of 0.135 MPa indicates a high sand production and an elevated sand control requirement. On the other hand, gas productivity is not closely related to cohesion, while it is more sensitive to permeability and the depressurization process. However, excessive or uncontrolled sand production can eventually impair the production operation. Therefore, although cohesion does not directly affect gas productivity, it is important to quantify its effect on sand production as sanding risks may damage the production operations and negatively affect gas productivity.

In addition, numerical results for a long-term production scenario based on the synthetic base case are provided and discussed. Figure 21 shows the plasticity and hydrate saturation results after 1 year of production. Compared with short-term results in Figure 10, the near-well plasticity becomes more significant and it is correlated with the hydrate dissociation area. The hydrate dissociation front also moves forward after 1 year.

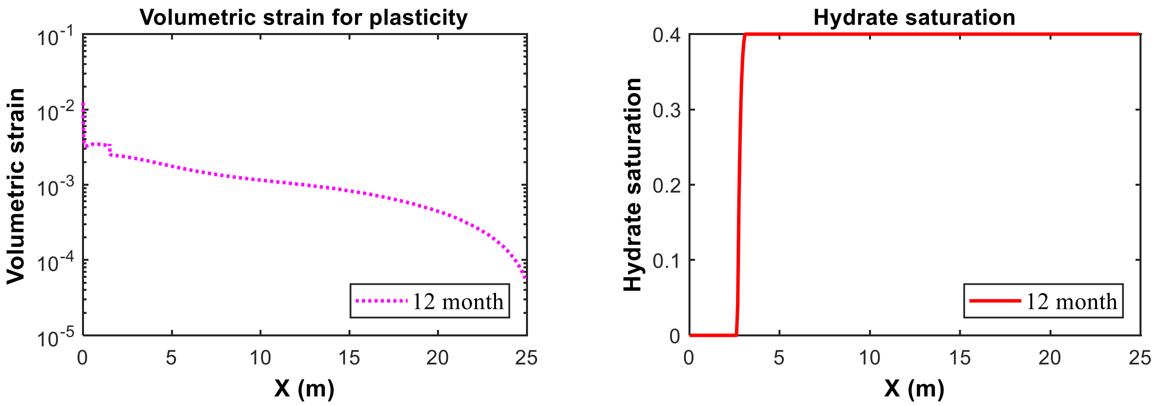

Figure 21. Plasticity and hydrate saturation distributions along y = 25 m after 1 year.

4. Conclusions

This study is focused on the coupled THMC behaviors induced by the depressurization through horizontal wellbore in methane-hydrate-bearing sediments. Based on rock failure and sand erosion mechanisms, sand production induced by methane exploitation is also considered in the study. The model is validated against a series of methane hydrate reservoir simulators. Several sensitivity analyses are carried out to examine the effects of permeability, cohesion, and time to reach the depressurization pressure on the THMC behaviors in the sediments and on the gas and sand production behaviors. In conclusion:

(1) A numerical model considering the coupling effects between thermal, hydraulic, mechanical, and chemical fields is introduced for the simulation of the depressurization process in methane-hydrate-bearing sediments. Hydrate dissociation fronts and temperature drop fronts simulated by the proposed model can be verified by other published models.
(2) The propagations of pressure drop and stress change are much faster than the movement of hydrate dissociation fronts and temperature drop fronts. This is because the fluid flow problem and the geomechanical problem are tightly coupled. In addition, temperature drop fronts move faster than hydrate dissociation fronts, as heat transport can occur even before hydrates are completely dissociated.
(3) Gas and sand production curves are not monotonical and oscillatory patterns are obtained. If the hydrocarbon drainage is stronger than the generation of methane from hydrate dissociation, the gas production rate can temporarily decrease. Sand production rates usually become stable after drastic sand production in the early stages.
(4) Gas production rates are sensitive to permeability and the time to reach the depressurization pressure, as these parameters directly govern the fluid flow in porous media. Gas production is not sensitive to rock mechanical properties such as cohesion. However, sand production is very sensitive to cohesion. Although cohesion does not directly affect gas productivity, excessive or uncontrolled sand production can impair the gas production operations and result in decreases in gas productivity in the field.

Author Contributions: X.G.: writing and simulation; Y.J.: conceptualization and reviewing; J.Z.: plotting and writing; J.L.: simulation; B.Z.: simulation; Q.W.: graphing and analysis; Q.J.: graphing and analysis. All authors have read and agreed to the published version of the manuscript.

Funding: This research was funded by the National Natural Science Foundation of China (No. U19B6003-05, No. 51904314, and No. 51991362), the CNPC Innovation Fund (No. 2021DQ02-0502), and the Open Fund of the State Key Laboratory of Shale Oil and Gas Enrichment Mechanisms and Effective Development (No. 21-GJ-KF-16). The APC was funded by the CNPC Innovation Fund.

Institutional Review Board Statement: Not applicable.

Informed Consent Statement: Not applicable.

Data Availability Statement: The data presented in this study are available in the figures within this article.

Acknowledgments: The authors acknowledge the financial support from the National Natural Science Foundation of China (No. U19B6003-05, No. 51904314, and No. 51991362), the CNPC Innovation Fund (No. 2021DQ02-0502), and the Open Fund of the State Key Laboratory of Shale Oil and Gas Enrichment Mechanisms and Effective Development (No. 21-GJ-KF-16).

Conflicts of Interest: The authors declare no conflict of interest.

References

1. Makogon, Y.F. Natural gas hydrates—A promising source of energy. *J. Nat. Gas Sci. Eng.* **2010**, *2*, 49–59. [CrossRef]
2. Sloan, E.D. Fundamental principles and applications of natural gas hydrates. *Nature* **2003**, *426*, 353–359. [CrossRef]
3. Boswell, R.; Collett, T.S. Current perspectives on gas hydrate resources. *Energy Environ. Sci.* **2011**, *4*, 1206–1215. [CrossRef]
4. Moridis, G.; Silpngarmlert, S.; Reagan, M.; Collett, T.; Zhang, K. Gas production from a cold, stratigraphically-bounded gas hydrate deposit at the Mount Elbert Gas Hydrate Stratigraphic Test Well, Alaska North Slope: Implications of uncertainties. *Mar. Pet. Geol.* **2011**, *28*, 517–534. [CrossRef]
5. Sung, W.; Lee, H.; Lee, H.; Lee, C. Numerical study for production performance of a methane hydrate reservoir stimulated by inhibitor injection. *Energy Sources* **2002**, *24*, 499–512. [CrossRef]
6. Moridis, G.J.; Reagan, M.T. Gas production from oceanic Class 2 hydrate accumulations. In Proceedings of the Offshore Technology Conference, OTC-18866, Houston, TX, USA, 30 April–3 May 2007.
7. White, M.; McGrail, P. Designing a pilot-scale experiment for the production of natural gas hydrates and sequestration of CO2 in class 1 hydrate accumulations. *Energy Procedia* **2009**, *1*, 3099–3106. [CrossRef]
8. Anderson, B.; Boswell, R.; Collett, T.S.; Farrell, H.; Ohtsuki, S.; White, M.; Zyrianova, M. Review of the findings of the Ignik Sikumi CO2-CH4 gas hydrate exchange field trial. In Proceedings of the 8th International Conference on Gas Hydrates, Beijing, China, 28 July–1 August 2014.
9. Yin, Z.; Chong, Z.R.; Tan, H.K.; Linga, P. Review of gas hydrate dissociation kinetic models for energy recovery. *J. Nat. Gas Sci. Eng.* **2016**, *35*, 1362–1387. [CrossRef]
10. Yamamoto, K.; Wang, X.-X.; Tamaki, M.; Suzuki, K. The second offshore production of methane hydrate in the Nankai Trough and gas production behavior from a heterogeneous methane hydrate reservoir. *RSC Adv.* **2019**, *9*, 25987–26013. [CrossRef]
11. Yu, T.; Guan, G.; Abudula, A.; Yoshida, A.; Wang, D.; Song, Y. Heat-assisted production strategy for oceanic methane hydrate development in the Nankai Trough, Japan. *J. Pet. Sci. Eng.* **2019**, *174*, 649–662. [CrossRef]
12. Ye, J.; Qin, X.; Xie, W.; Lu, H.; Ma, B.; Qiu, H.; Liang, J.; Lu, J.A.; Kuang, Z.; Lu, C.; et al. Main progress of the second gas hydrate trial production in the South China Sea. *Geol. China* **2020**, *47*, 557–568.
13. Zhu, H.; Xu, T.; Yuan, Y.; Feng, G.; Xia, Y.; Xin, X. Numerical analysis of sand production during natural gas extraction from unconsolidated hydrate-bearing sediments. *J. Nat. Gas Sci. Eng.* **2020**, *76*, 103229. [CrossRef]
14. Rahmati, H.; Jafarpour, M.; Azadbakht, S.; Nouri, A.; Vaziri, H.; Chan, D.; Xiao, Y. Review of Sand Production Prediction Models. *J. Pet. Eng.* **2013**, *2013*, 864981. [CrossRef]
15. Papamichos, E.; Vardoulakis, I.; Tronvoll, J.; Skjærstein, A. Volumetric sand production model and experiment. *Int. J. Numer. Anal. Methods Geomech.* **2001**, *25*, 789–808. [CrossRef]
16. Jung, J.W.; Santamarina, J.C. Hydrate adhesive and tensile strengths. *Geochem. Geophys. Geosyst.* **2011**, *12*. [CrossRef]
17. Sánchez, M.; Santamarina, C.; Teymouri, M.; Gai, X. Coupled Numerical Modeling of Gas Hydrate-Bearing Sediments: From Laboratory to Field-Scale Analyses. *J. Geophys. Res. Solid Earth* **2018**, *123*, 10326–10348. [CrossRef]
18. Younessi, A.; VRasouli Wu, B. Sand production simulation under true-triaxial stress conditions. *Int. J. Rock Mech. Min. Sci.* **2013**, *61*, 130–140. [CrossRef]
19. Uchida, S.; Klar, A.; Yamamoto, K. Sand production modeling of the 2013 Nankai offshore gas production test. In Proceedings of the 1st International Conference on Energy Geotechnics, Kiel, Germany, 29–31 August 2016.
20. Li, X.; Feng, Y.; Gray, K.E. A hydro-mechanical sand erosion model for sand production simulation. *J. Pet. Sci. Eng.* **2018**, *166*, 208–224. [CrossRef]

21. Yan, C.; Li, Y.; Cheng, Y.; Wang, W.; Song, B.; Deng, F.; Feng, Y. Sand production evaluation during gas production from natural gas hydrates. *J. Nat. Gas Sci. Eng.* **2018**, *57*, 77–88. [CrossRef]
22. Ding, J.; Cheng, Y.; Yan, C.; Song, B.; Sun, H.; Teng, F. Experimental study of sand control in a natural gas hydrate reservoir in the South China sea. *Int. J. Hydrogen Energy* **2019**, *44*, 23639–23648. [CrossRef]
23. Ding, J.; Cheng, Y.; Yan, C.; Lu, C.; Li, Y.; Xue, M. Numerical simulation on sand production in the exploitation process of gas hydrates based on skeleton failure of reservoirs. *J. Nat. Gas Sci. Eng.* **2021**, *94*, 104052. [CrossRef]
24. Rutqvist, J.; Moridis, G.J. Numerical studies on the geomechanical stability of hydrate-bearing sediments. In Proceedings of the Offshore Technology Conference, Paper OTC-18860-MS. Houston, TX, USA, 30 April–3 May 2007.
25. Kim, J.; Moridis, G.J.; Yang, D.; Rutqvist, J. Numerical Studies on Two-Way Coupled Fluid Flow and Geomechanics in Hydrate Deposits. *SPE J.* **2012**, *17*, 485–501. [CrossRef]
26. Guo, X.; Jin, Y.; Zi, J.; Lin, B. Numerical Investigation of the Gas Production Efficiency and Induced Geomechanical Responses in Marine Methane Hydrate-Bearing Sediments Exploited by Depressurization through Hydraulic Fractures. *Energy Fuels* **2021**, *35*, 18441–18458. [CrossRef]
27. Yoneda, J.; Masui, A.; Konno, Y.; Jin, Y.; Egawa, K.; Kida, M.; Ito, T.; Nagao, J.; Tenma, N. Mechanical properties of hydrate-bearing turbidite reservoir in the first gas production test site of the Eastern Nankai Trough. *Mar. Pet. Geol.* **2015**, *66*, 471–486. [CrossRef]
28. Li, Y.; Cheng, Y.; Yan, C.; Song, L.; Liu, H.; Tian, W.; Ren, X. Mechanical study on the wellbore stability of horizontal wells in natural gas hydrate reservoirs. *J. Nat. Gas Sci. Eng.* **2020**, *79*, 103359. [CrossRef]
29. Ning, F.; Sun, J.; Liu, Z.; Peng, L.; Zhang, L.; Hu, G.; Wu, N.; Lu, H.; Lu, J.A.; Liang, J. Prediction of sand production in gas recovery from the Shenhu hydrate reservoir by depressurization. In Proceedings of the 9th International Conference of Gas Hydrate (ICGH9), Denver, CO, USA, 25–30 June 2017.
30. Jin, G.; Lei, H.; Xu, T.; Xin, X.; Yuan, Y.; Xia, Y.; Juo, J. Simulated geomechanical responses to marine methane hydrate recovery using horizontal wells in the Shenhu area, South China Sea. *Mar. Pet. Geol.* **2018**, *92*, 424–436. [CrossRef]
31. Satter, A.; Iqbal, G.M. *Reservoir Engineering: The Fundamentals, Simulation, and Management of Conventional and Unconventional Recoveries*; Gulf Professional Publishing: Houston, TX, USA, 2015.
32. Guo, X.; Jin, Y.; Lin, B. A Parametric Study of Coupled Hydromechanical Behaviors Induced by Shallow Water Flow in Shallow Sediments in Deepwater Drilling Based on Numerical Modeling. *Geofluids* **2020**, 2592693. [CrossRef]
33. Guo, X.; Song, H.; Killough, J.; Du, L.; Sun, P. Numerical investigation of the efficiency of emission reduction and heat extraction in a sedimentary geothermal reservoir: A case study of the Daming geothermal field in China. *Environ. Sci. Pollut. Res.* **2018**, *25*, 4690–4706. [CrossRef]
34. Zhi, D.; Guo, X.; Wang, W.; Jin, Y.; Liu, C.; Chen, G.; Wang, Z. Fracturing and production analysis of the efficacy of hydraulic fracture stage reduction in the improvement of cost-effectiveness in shale oil development: A case study of Jimsar shale oil, China. *Energy Sci. Eng.* **2021**, *9*, 1337–1348. [CrossRef]
35. Walsh, M.P.; Lake, L.W. Applying fractional flow theory to solvent flooding and chase fluids. *J. Pet. Sci. Eng.* **1989**, *2*, 281–303. [CrossRef]
36. Sun, X.; Mohanty, K.K. Kinetic simulation of methane hydrate formation and dissociation in porous media. *Chem. Eng. Sci.* **2006**, *61*, 3476–3495. [CrossRef]
37. Ju, X.; Liu, F.; Fu, P.; White, M.D.; Settgast, R.R.; Morris, J.P. Gas Production from Hot Water Circulation through Hydraulic Fractures in Methane Hydrate-Bearing Sediments: THC-Coupled Simulation of Production Mechanisms. *Energy Fuels* **2020**, *34*, 4448–4465. [CrossRef]
38. De La Fuente, M.; Vaunat, J.; Marín-Moreno, H. Thermo-Hydro-Mechanical Coupled Modeling of Methane Hydrate-Bearing Sediments: Formulation and Application. *Energies* **2019**, *12*, 2178. [CrossRef]
39. Kim, H.; Bishnoi, P.; Heidemann, R.; Rizvi, S. Kinetics of methane hydrate decomposition. *Chem. Eng. Sci.* **1987**, *42*, 1645–1653. [CrossRef]
40. Moridis, G.J. Numerical Studies of Gas Production From Methane Hydrates. *SPE J.* **2003**, *8*, 359–370. [CrossRef]
41. Tishchenko, P.; Hensen, C.; Wallmann, K.; Wong, C.S. Calculation of the stability and solubility of methane hydrate in seawater. *Chem. Geol.* **2005**, *219*, 37–52. [CrossRef]
42. Bathe, K. *Finite Element Procedures*; Prentice-Hall: Englewood Cliffs, NJ, USA, 1996.
43. Kim, J.; Moridis, G.J. Modeling And Numerical Simulation For Coupled Flow And Geomechanics In Composite Gas Hydrate Deposits. In Proceedings of the 46th U.S. Rock Mechanics/Geomechanics Symposium, Chicago, IL, USA, 24–27 June 2017.
44. Kim, J. A new numerically stable sequential algorithm for coupled finite-strain elastoplastic geomechanics and flow. *Comput. Methods Appl. Mech. Eng.* **2018**, *335*, 538–562. [CrossRef]
45. Pham, S.T.; Riveiro, A. Estimation of Sand Production Rate Using Geomechanical and Hydromechanical Models. *Adv. Mater. Sci. Eng.* **2017**, *2017*, 2195404. [CrossRef]
46. Papamichos, E.; Walle, L.E.; Berntsen, A.N.; Stenebråten, J.F. Sand Mass Production in True Triaxial Borehole Tests. In Proceedings of the 53rd U.S. Rock Mechanics/Geomechanics Symposium, ARMA-2019-0238, New York, NY, USA, 23–26 June 2019.
47. Anderson, B.; Hancock, S.; Wilson, S.; Enger, C.; Collett, T.; Boswell, R.; Hunter, R. Formation pressure testing at the Mount Elbert Gas Hydrate Stratigraphic Test Well, Alaska North Slope: Operational summary, history matching, and interpretations. *Mar. Pet. Geol.* **2011**, *28*, 478–492. [CrossRef]

48. White, M.; Kneafsey, T.; Seol, Y.; Waite, W.; Uchida, S.; Lin, J.; Myshakin, E.; Gai, X.; Gupta, S.; Reagan, M.; et al. An international code comparison study on coupled thermal, hydrologic and geomechanical processes of natural gas hydrate-bearing sediments. *Mar. Pet. Geol.* **2020**, *120*, 104566. [CrossRef]
49. Liu, X.; Xing, L.; Qin, Z.; Liu, H. The Sensitive Properties of Hydrate Reservoirs Based on Seismic Stereoscopic Detection Technology. *Acta Geol. Sin. (Engl. Ed.)* **2020**, *94*, 530–544. [CrossRef]
50. Kurihara, M.; Sato, A.; Funatsu, K.; Ouchi, H.; Yamamoto, K.; Numasawa, M.; Ebinuma, T.; Narita, H.; Masuda, Y.; Dallimore, S.R.; et al. Analysis of Production Data for 2007/2008 Mallik Gas Hydrate Production Tests in Canada. In Proceedings of the International Oil and Gas Conference and Exhibition in China, Beijing, China, 8–10 June 2010.
51. Yamamoto, K.; Terao, Y.; Fujii, T.; Ikawa, T.; Seki, M.; Matsuzawa, M.; Kanno, T. Operational overview of the first offshore production test of methane hydrates in the Eastern Nankai Trough. In Proceedings of the Offshore Technology Conference, Houston, TX, USA, 5–8 May 2014; pp. 1–15.